Available online at www.sciencedirect.com
ScienceDirect
Trans. Nonferrous Met. Soc. China 35(2025) 3795−3812
Transactions of Nonferrous Metals Society of China
www.tnmsc.cn

Development of Co−Ni−Ti−V superalloys with exceptional high-temperature strength based on phase diagram

Jian-ping LE[1,2], Jin-bin ZHANG[1,2], Yu-peng ZHANG[1,2], Yi-hui GUO[1,2], Yong LU[1,2], Cui-ping WANG[1,2], Xing-jun LIU[3]

1. Fujian Provincial Key Laboratory of Materials Genome Engineering, College of Materials, Xiamen University, Xiamen 361005, China;
2. Xiamen Key Laboratory of High Performance Metals and Materials, Xiamen University, Xiamen 361005, China;
3. Institute of Materials Genome and Big Data, Harbin Institute of Technology, Shenzhen 518055, China

Received 8 March 2024; accepted 10 December 2024

Abstract: The Co−Ni−Ti−V quaternary phase diagrams within the Co−Ni-rich region were investigated using the electron probe X-ray micro-analyzer (EPMA) and X-ray diffraction (XRD). Three isothermal sections corresponding to the Co−10Ni−Ti−V, Co−15Ni−Ti−V, and Co−20Ni−Ti−V quaternary systems at 1000 °C were experimentally established. The results indicate that increasing Ni content markedly broadens the γ (α-Co) and γ' (Co_3Ti) two-phase regions. Based on the Co−Ni−Ti−V phase diagram, alloys with high γ' solvus temperature were designed, and their comprehensive properties, including γ' coarsening behavior and mechanical properties, were thoroughly investigated. Compared to Co−Ti−based superalloys, the Co−20Ni−10Ti−10V alloy exhibits lower coarsening rates of γ' precipitates and γ/γ' lattice mismatch. Notably, it possesses exceptional high-temperature mechanical properties, with a yield strength of 508 MPa at 1000 °C. This superior performance is primarily attributed to the presence of a high density of stacking fault shear.

Key words: Co−Ni−Ti−V; phase equilibria; partition coefficient; coarsening rate; mechanical property

1 Introduction

Superalloys have gained significant attention with the continuous development of the aerospace industry [1−3]. In the previous century, Ni-based superalloys were widely used due to their excellent high-temperature strength, corrosion resistance, and creep resistance [4,5]. However, the melting temperature of Ni-based superalloys has been close to the melting point of Ni, limiting the design of next-generation gas turbines [6,7]. As a result, it is necessary to develop alternative alloy systems [8,9]. In particular, Co-based superalloys have garnered significant interest owing to their exceptionally high theoretical melting temperatures and the presence of the γ' strengthening phase [10,11].

The Co−Ti binary system is reported to have stable γ (disordered fcc-Co) and γ' (ordered $L1_2$ Co_3Ti) phases [12,13], and the potential to develop superalloys with stable γ/γ' two-phase microstructure. However, the use of Co−Ti alloys is limited by several properties. The maximum solubility of Ti in fcc-Co is 12 at.%, which can only generate approximately 20 vol.% of γ' at 900 °C. In addition, the large lattice mismatch between the γ' and γ phases and the rapid coarsening rate of γ' precipitation in Co−Ti binary alloys, severely reduces the microstructural stability and the service life at elevated temperatures. In recent years, significant breakthroughs have been made in the design of Co−Ti-based superalloys. The addition of

Corresponding author: Yong LU, Tel: +86-13950168391, E-mail: luyong@xmu.edu.cn; Cui-ping WANG, E-mail: wangcp@xmu.edu.cn; Xing-jun LIU, E-mail: xjliu@hit.edu.cn

https://doi.org/10.1016/S1003-6326(25)66913-5

third elements such as V [14,15], Mo [16,17], W [18], Cr [17,19], Re [20,21] and Ta [13] to the Co−Ti alloys enhances the thermal stability, high-temperature mechanical properties, and microstructure stability. However, the performance of the newly developed Co−Ti-based ternary superalloys can hardly meet the expectation, highlighting the need for further optimization of Co−Ti-based alloys. Compared to Co−Ti−X (X= Mo, W, Cr, Re) alloys, the Co−Ti−V systems exhibit a large γ/γ' two-phase region and display remarkable stability of the $\gamma'(Co_3Ti)$ phase [15]. In addition, Ni plays a crucial role as an important alloying element in Co-based high-performance alloys [22−25]. The outstanding properties of the Co−20Ni−10Ti−4V alloy demonstrate the promising potential for the further development of Co−Ni−Ti−V alloys [26]. However, there is currently a lack of research on the γ/γ' dual-phase region of Co−Ni−Ti−V superalloys, which poses a challenge in providing valuable support for the next stage of alloy development.

The aim of this study is to investigate the phase equilibrium of the cobalt-rich region in the Co−Ni−Ti−V system at 1000 °C. The influence of Ni content on the γ' solvus temperature and the γ/γ' phase partition coefficient was studied. Additionally, the morphology of γ' precipitation, the coarsening rate of γ' precipitation, the lattice mismatch between the γ and γ' phases, and the mechanical properties were explored.

2 Experimental

Button ingots, weighing approximately 30 g, were prepared by melting raw materials of Co, Ti, Ni, and V (with a purity of at least 99.99 wt.%) using an arc melting unit under a high-purity Ar atmosphere. Additionally, ingots weighing approximately 90 g were prepared using arc melting for mechanical property tests. To ensure homogeneity, the ingots were melted at least 5 times. Afterwards, the ingots were cut into appropriately-sized specimens for heat treatment with a wire-cutting machine.

The samples that require heat treatment must be sealed in a vacuumed quartz tube. Firstly, the specimens are subjected to homogenization annealing at temperatures of 1150−1200 °C for 48 h. Subsequently, a further annealing was performed at 750 °C. Specimens for equilibrium treatment at 1000 °C must undergo cold rolling with a reduction rate of 60% to promote atomic diffusion. After heat treatment, the samples were quenched in ice water.

The microstructure of γ/γ' phase was observed using a field emission scanning electron microscope (FE-SEM, SU70, Hitachi, Japan) and the composition of the γ/γ' phase was determined using an electron probe X-ray microanalyzer (EPMA, JXA−8100, JEOL). A JEM−2100Plus transmission electron microscope (TEM) was used for the observation of the γ' phase and dislocation analysis. The average size and area fraction of the γ' phase were measured using Image J software. Assuming cubic-shaped γ' morphology, the average size (a) was used to determine γ' particle average radius (r) through $r=a\cdot(3/4\pi)^{1/3}$. Finally, the experimental data were analyzed by linear regression using Origin2021 software.

The phase transition temperature of the Co-based superalloys was determined using a Netzsch 404F3 high-temperature differential scanning calorimeter (DSC) at a heating rate of 20 °C/min. The crystal structure of the specimens was determined using a Bruker D8 XRD and the experimental data were analyzed using Jade 6.0 software. The hardness was measured using an MVK-H1 hardness testing machine from Akashi, Japan, with the load of 0.5 kg. Density measurements were performed at room temperature using ASTM B311-08. For the compression test, cylindrical specimens with a diameter of 4 mm and a height of 6 mm were first prepared using the DK7725 wire-cutting machine. Subsequently, after heat treatment, the specimens were tested using the WDW−100E testing machine at a strain rate of $1\times10^{-4}\ s^{-1}$. The temperature change for compression test was maintained within ±5 °C.

3 Results and discussion

3.1 Phase equilibria of Co−Ni−Ti−V alloys at 1000 °C

3.1.1 Phase equilibrium of Co−Ni−X (X=V, Ti) ternary alloys

In order to determine the phase equilibria of the Co−Ni−Ti−V, experimental studies on the Co−Ni−X (X=V, Ti) ternary alloys were carried out as a priority in this study. As shown in Fig. 1, the EPMA images depict the Co−10Ni−20V, Co−10Ni−

35V, Co−10Ni−30Ti, and Co−10Ni−18Ti ternary alloys (Unless stated otherwise, all compositions discussed in this work are expressed in at.%) annealed at 1000 °C for 75 d, respectively. Table 1 summarizes the equilibrium compositions of Co−Ni−X (X=V, Ti) ternary alloys at 1000 °C as determined by EPMA, and Table S1 in Supplementary Materials (SM) summarizes the corresponding stable solid phases and their crystallographic data. Additionally, Fig. 2 shows the X-ray diffraction results of typical Co−Ni−X (X=V, Ti) ternary alloys annealed at 1000 °C for 75 d.

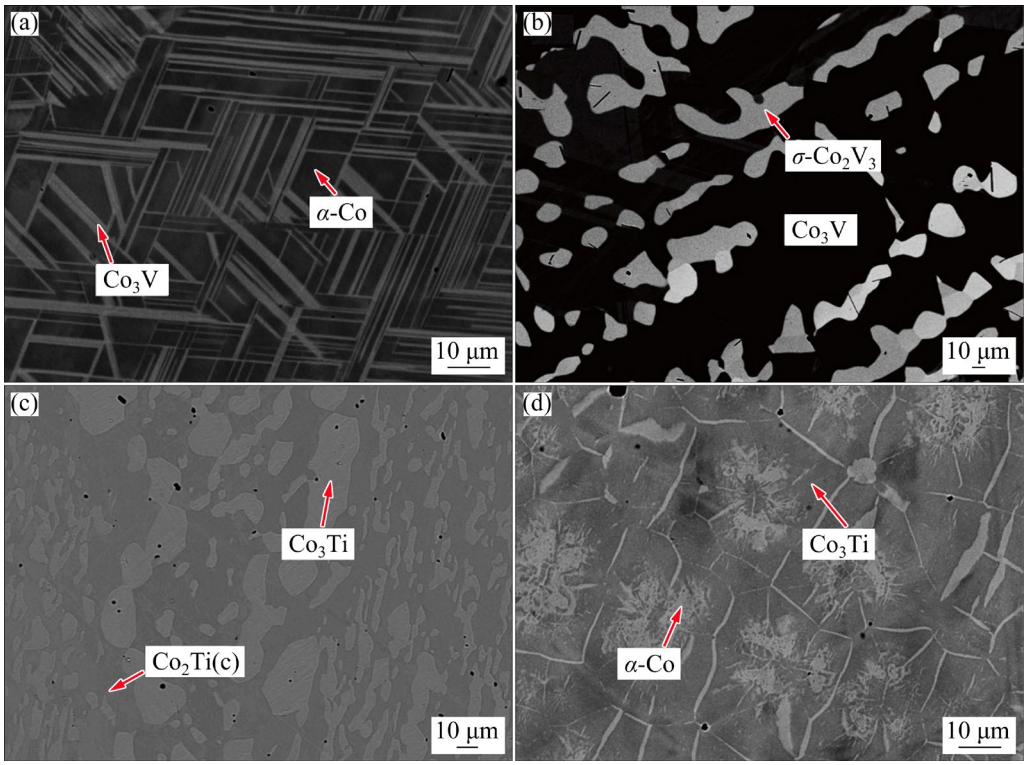

Fig. 1 EPMA images of Co−10Ni−20V (a), Co−10Ni−35V (b), Co−10Ni−30Ti (c), and Co−10Ni−18Ti (d) alloys annealed at 1000 °C for 75 d

Table 1 Equilibrium compositions of Co−Ni−X (X=V, Ti) ternary alloys annealed at 1000 °C

Alloy	Annealing time/d	Equilibria	Composition/at.%					
		Phase 1/Phase 2	Phase 1			Phase 2		
			Ni	Ti	V	Ni	Ti	V
Co−10Ni−20V	75	α-Co/Co_3V	9.7	0	19.9	9.3	0	23.6
Co−10Ni−35V	75	Co_3V/σ-Co_2V_3	11.2	0	32.9	6.6	0	41.7
Co−10Ni−18Ti	75	α-Co/Co_3Ti	9.4	11.9	0	12.5	20.8	0
Co−10Ni−30Ti	75	Co_3Ti/Co_2Ti(c)	11.3	26.5	0	5.0	33.2	0
Co−15Ni−20V	75	α-Co/Co_3V	14.7	0	20.6	13.8	0	24.0
Co−15Ni−35V	75	Co_3V/σ-Co_2V_3	15.7	0	33.6	9.7	0	42.3
Co−15Ni−18Ti	75	α-Co/Co_3Ti	13.4	11.3	0	17.8	21.5	0
Co−15Ni−30Ti	75	Co_3Ti/Co_2Ti(c)	24.3	26.4	0	9.5	33.0	0
Co−20Ni−20V	75	α-Co/Co_3V	20.4	0	20.2	19.0	0	23.5
Co−20Ni−35V	75	Co_3V/σ-Co_2V_3	20.6	0	34.2	13.1	0	43.4
Co−20Ni−18Ti	75	α-Co/Co_3Ti	19.1	10.6	0	24.8	21.7	0

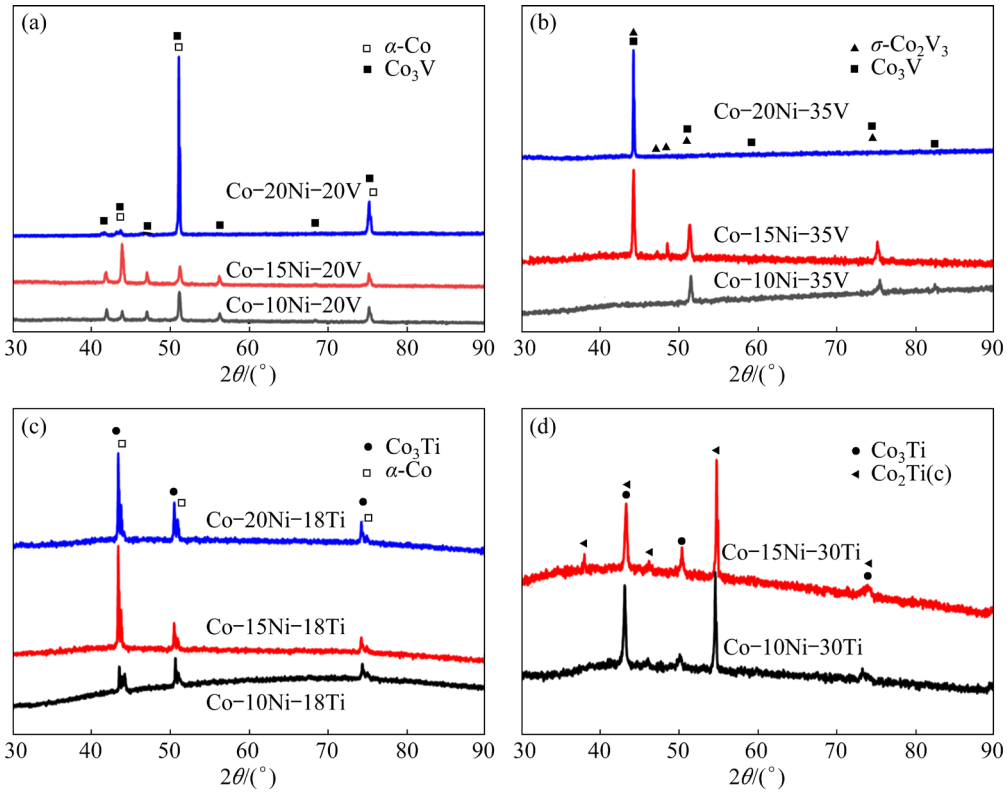

Fig. 2 XRD patterns of alloys after annealing at 1000 °C for 75 d

The Co−10Ni−20V alloy, annealed at 1000 °C for 75 d, exhibits a typical two-phase equilibrium, as shown in Fig. 1(a). The microstructure reveals the black phase as α-Co and the gray needle phase as Co_3V. The corresponding XRD pattern is shown in Fig. 2(a). The equilibrium microstructure of the Co−10Ni−35V alloy annealed at 1000 °C for 75 d is shown in Fig. 1(b). The corresponding XRD pattern is shown in Fig. 2(b). The Co_3V phase appears black, whereas the σ-Co_2V_3 phase exhibits two colors, including white and gray, influenced by factors such as crystal orientation. Notably, the σ-Co_2V_3 phase is uniformly distributed throughout the Co_3V matrix. Figure 1(c) displays the microstructure of the Co−10Ni−30Ti alloy after annealing at 1000 °C for 75 d. The gray phase corresponds to Co_2Ti(c), while the white phase represents the Co_3Ti phase. Figure 2(c) depicts the respective XRD pattern. As shown in Fig. 1(d), the two-phase equilibrium of α-Co and Co_3Ti can be observed in the Co−10Ni−18Ti alloy annealed at 1000 °C for 75 d. The corresponding XRD pattern can be seen in Fig. 2(d).

3.1.2 Phase equilibria of Co−Ni−Ti−V quaternary alloys

Figure 3 shows the equilibrium microstructure of the Co−10Ni−2Ti−19V, Co−20Ni−11Ti−20V, Co−10Ni−10Ti−10V, Co−15Ni−17Ti−18V, Co−10Ni−25Ti−5V, Co−15Ni−25Ti−5V, Co−20Ni−25Ti−5V and Co−10Ni−9.5Ti−17.5V quaternary alloys at 1000 °C, respectively. Table 2 presents the equilibrium compositions of Co−Ni−Ti−V alloys at 1000 °C, including the composition ranges of α-Co, Co_3V, Co_3Ti, σ-Co_2V_3, Co_2Ti(c), and (Co, Ni)Ti phases. Figure 4 shows the XRD results of typical Co−Ti−Ni−V quaternary alloys annealed at 1000 °C for an extended period of time. In addition, the stable solid phases and their crystallographic data are summarized in Table S1 of SM.

Figure 3(a) shows the equilibrium microstructure of the Co−10Ni−2Ti−19V alloy after annealing at 1000 °C for 75 d, determined as α-Co and Co_3V two-phase microstructure by using XRD analysis (Fig. 4(a)). The equilibrium microstructure of the Co−20Ni−11Ti−20V alloy at 1000 °C, as shown in Fig. 3(b), consists of two phases of dark gray Co_3V and light gray σ-Co_2V_3 phases as determined by XRD (Fig. 4(b)). In the Co−10Ni−10Ti−10V alloy annealed at 1000 °C for 75 d, a two-phase equilibrium microstructure was observed (Fig. 3(c)), and the two phases were determined to

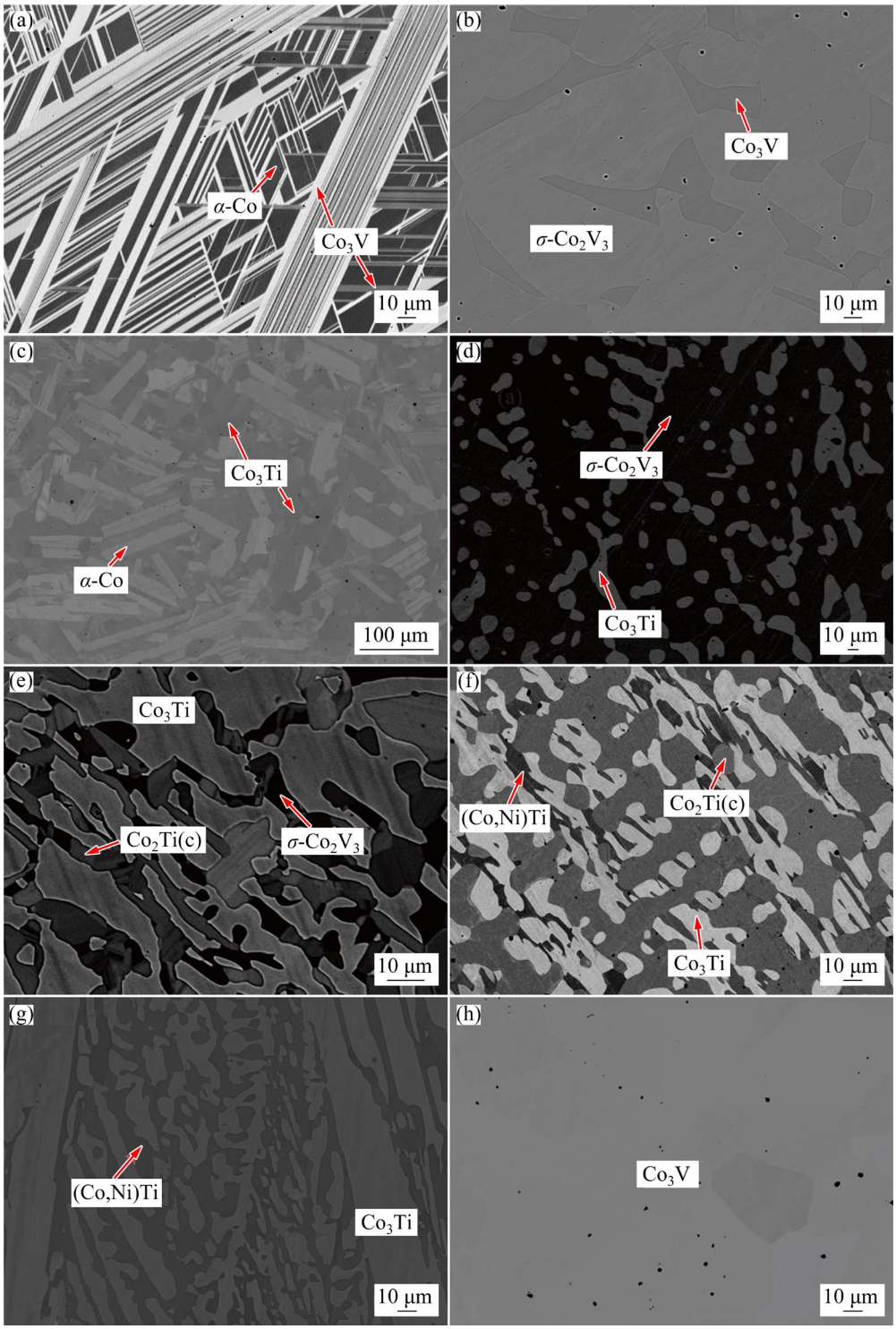

Fig. 3 EPMA images of Co−10Ni−2Ti−19V (a), Co−20Ni−11Ti−20V (b), Co−10Ni−10Ti−10V (c), Co−15Ni−17Ti−18V (d), Co−10Ni−25Ti−5V (e), Co−15Ni−30Ti−1V (f), Co−20Ni−25Ti−5V (g), and Co−10Ni−9.5Ti−17.5V (h) alloys cold-rolled at reduction rate of 50% and annealed at 1000 °C

be the α-Co and Co_3Ti phases, respectively, by XRD analysis (Fig. 4(c)). After annealing the Co−15Ni−17Ti−18V alloy at 1000 °C for 75 d, a two-phase equilibrium was observed, as shown in Fig. 3(d). The black phase was identified as Co_3Ti, while the white phase was identified as σ-Co_2V_3. The corresponding XRD pattern is shown in Fig. 4(d). Notably, the σ-Co_2V_3 phase was uniformly distributed in the black matrix of the Co_3Ti phase. The three-phase equilibrium was

Table 2 Equilibrium compositions of Co−Ni−Ti−V quaternary alloys annealed at 1000 °C

Alloy	Annealed time/d	Equilibria	Composition/at.%								
		Phase 1/Phase 2/Phase 3	Phase 1			Phase 2			Phase 3		
			Ni	Ti	V	Ni	Ti	V	Ni	Ti	V
Co−10Ni−15Ti−2V	90	α-Co/Co_3Ti	8.5	11.0	1.9	11.1	18.9	2.3			
Co−10Ni−10Ti−10V	75	α-Co/Co_3Ti	8.3	6.7	9.2	10.1	12.5	10.5			
Co−10Ni−13Ti−20V	75	Co_3V/σ-Co_2V_3	9.7	11.1	14.5	4.9	16.5	24.4			
Co−10Ni−2Ti−19V	75	α-Co/Co_3V	9.5	1.3	18.1	9.5	2.8	21.1			
Co−10Ni−13Ti−5V	75	α-Co/Co_3Ti	8.3	8.7	5.2	10.2	15.9	6.1			
Co−10Ni−6Ti−17V	90	Co_3V	9.9	6.3	16.8						
Co−10Ni−8Ti−15V	75	Co_3V	9.8	8.1	15.5						
Co−10Ni−7Ti−15V	75	Co_3V	9.9	7.2	15.3						
Co−10Ni−9Ti−13V	75	Co_3V	9.8	9.7	13.9						
Co−10Ni−8Ti−14V	75	Co_3V	9.9	8.8	14.7						
Co−10Ni−8.5Ti−18.5V	90	Co_3V	9.8	8.5	18.2						
Co−10Ni−9.5Ti−17.5V	90	Co_3V	10.1	9.2	17.2						
Co−10Ni−11Ti−15V	75	Co_3Ti	9.8	11.4	15.3						
Co−10Ni−11Ti−20V	120	Co_3V/σ-Co_2V_3	12.2	10.5	18.4	6.3	15.4	25.4			
Co−10Ni−15Ti−18V	120	Co_3Ti/σ-Co_2V_3	12.2	12.7	15.5	6.0	18.4	22.2			
Co−10Ni−17Ti−18V	120	Co_3Ti/σ-Co_2V_3	14.9	13.8	14.4	7.2	20.0	21.1			
Co−10Ni−13Ti−18V	75	Co_3Ti/σ-Co_2V_3	10.1	12.0	16.2	5.0	18.4	22.4			
Co−10Ni−12Ti−16V	75	Co_3Ti	9.7	12.0	16.4						
Co−10Ni−25Ti−12V	120	σ-Co_2V_3	9.0	27.3	13.2						
Co−10Ni−22Ti−10V	75	Co_3Ti /σ-Co_2V_3	12.1	18.2	9.1	5.3	28.2	12.3			
Co−10Ni−25Ti−5V	120	Co_3Ti/σ-Co_2V_3/Co_2Ti(c)	13.2	20.8	6.2	6.1	32.5	8.0	5.8	31.1	3.4
Co−15Ni−15Ti−2V	75	α-Co/Co_3Ti	12.2	9.8	1.9	18.2	17.5	2.1			
Co−15Ni−12Ti−12V	75	α-Co/Co_3Ti	12.4	5.7	9.8	15.1	12.3	11.2			
Co−15Ni−2Ti−19V	75	α-Co/Co_3V	14.9	1.34	18.4	14.4	3.1	20.6			
Co−15Ni−10Ti−10V	75	α-Co/Co_3Ti	12.4	5.8	9.6	15.1	12.2	10.9			
Co−15Ni−13Ti−5V	75	α-Co/Co_3Ti	12.5	8.2	5.2	15.8	16.5	5.6			
Co−15Ni−6Ti−17V	75	Co_3V	14.8	6.2	17.1						
Co−15Ni−10Ti−15V	75	Co_3V	15.0	10.4	15.3						
Co−15Ni−11Ti−5V	75	Co_3V	14.9	10.8	15.1						
Co−15Ni−7Ti−14V	75	α-Co/Co_3V	13.4	3.4	13.2	15.1	8.8	15.0			
Co−15Ni−9Ti−14V	75	Co_3V	14.2	9.3	15.6						
Co−15Ni−10Ti−13.5V	75	Co_3V	14.5	10.3	14.9						
Co−15Ni−8.5Ti−18.5V	75	Co_3V	15.2	8.3	18.4						

To be continued

Continued

Alloy	Annealed time/d	Equilibria	Composition/at.%								
		Phase 1/Phase 2/Phase 3	Phase 1			Phase 2			Phase 3		
			Ni	Ti	V	Ni	Ti	V	Ni	Ti	V
Co−15Ni−9.5Ti−17.5V	75	Co_3V	15.3	9.6	17.8						
Co−15Ni−11Ti−20V	75	Co_3V/σ-Co_2V_3	16.1	10.4	19.0	8.1	13.8	27.4			
Co−15Ni−15Ti−18V	75	Co_3Ti/σ-Co_2V_3	18.0	12.9	15.6	8.5	18.5	23.2			
Co−15Ni−17Ti−18V	75	Co_3Ti/σ-Co_2V_3	20.5	14.7	13.7	9.6	19.7	22.2			
Co−15Ni−12Ti−18V	75	Co_3V/σ-Co_2V_3	15.3	11.2	17.1	7.6	15.3	25.9			
Co−15Ni−12Ti−16V	75	Co_3V/σ-Co_2V_3	15.2	12.0	15.7	7.4	17.2	24.3			
Co−15Ni−25Ti−12V	75	Co_3Ti/σ-Co_2V_3	24.3	19.7	7.9	10.9	27.9	13.8			
Co−15Ni−25Ti−5V	75	Co_3Ti/(Co,Ni)Ti	17.4	22.5	4.7	7.7	34.2	6.6			
Co−15Ni−32Ti−10V	90	Co_3Ti/σ-Co_2V_3	27.5	12.7	5.4	11.3	32.1	10.0			
Co−15Ni−33Ti−10V	90	σ-Co_2V_3	14.4	32.4	10.7						
Co−15Ni−36Ti−10V	75	σ-Co_2V_3	14.8	35.7	10.2						
Co−15Ni−30Ti−1V	25	Co_3Ti/Co_2Ti(c)/(Co,Ni)Ti	24.3	25.0	1.4	9.3	32.6	1.0	9.9	39.1	2.2
Co−15Ni−28Ti−3V	25	Co_3Ti/(Co,Ni)Ti	18.5	24.1	3.0	8.1	36.7	4.3			
Co−20Ni−15Ti−2V	75	α-Co/Co_3Ti	15.4	10.0	2.1	24.3	20.7	2.3			
Co−20Ni−10Ti−5V	75	α-Co/Co_3Ti	22.8	17.3	6.5	17.7	7.7	5.5			
Co−20Ni−10Ti−10V	75	α-Co/Co_3Ti	17.4	6.6	9.9	20.4	13.7	11.0			
Co−20Ni−10Ti−15V	75	Co_3V	20.0	9.8	15.2						
Co−20Ni−6Ti−17V	75	Co_3V	19.9	6.3	17.3						
Co−20Ni−9Ti−14V	90	Co_3V	19.7	9.4	14.9						
Co−20Ni−12Ti−14V	90	Co_3V	20.1	11.4	14.3						
Co−20Ni−8.5Ti−18.5V	75	Co_3V	20.1	9.0	19.2						
Co−20Ni−9.5Ti−19.5V	75	Co_3V	20.8	10.2	20.1						
Co−20Ni−12Ti−15V	75	Co_3V	19.6	12.6	15.1						
Co−20Ni−11Ti−20V	75	Co_3V/σ-Co_2V_3	20.9	10.0	20.0	12.9	15.3	27.5			
Co−20Ni−15Ti−18V	75	Co_3V/σ-Co_2V_3	20.7	12.8	17.1	10.2	15.2	27.0			
Co−20Ni−15Ti−17V	75	Co_3Ti/σ-Co_2V_3	22.9	15.2	14.2	11.0	17.5	24.3			
Co−20Ni−5Ti−30V	75	Co_3V/σ-Co_2V_3	22.8	6.7	24.4	12.7	2.1	41.5			
Co−20Ni−18Ti−16V	75	Co_3Ti/σ-Co_2V_3	32.7	17.8	11.1	15.5	20.5	21.6			
Co−20Ni−20Ti−13V	75	Co_3Ti/σ-Co_2V_3	24.8	18.5	10.3	11.0	22.3	19.3			
Co−20Ni−25Ti−12V	75	Co_3Ti/σ-Co_2V_3	34.5	21.3	6.2	15.4	28.2	14.2			
Co−20Ni−28Ti−5V	75	Co_3Ti/σ-Co_2V_3	25.7	22.9	3.8	10.6	34.9	6.9			
Co−20Ni−25Ti−5V	75	Co_3Ti/(Co,Ni)Ti	26.9	22.5	4.1	11.9	34.3	7.2			
Co−20Ni−27Ti−6V	75	Co_3Ti/(Co,Ni)Ti	25.7	22.2	4.8	11.0	33.7	8.3			
Co−20Ni−32Ti−10V	75	Co_3Ti/σ-Co_2V_3	33.9	22.4	5.0	14.7	29.9	12.4			
Co−20Ni−36Ti−10V	75	(Co,Ni)Ti	19.6	33.7	9.7						

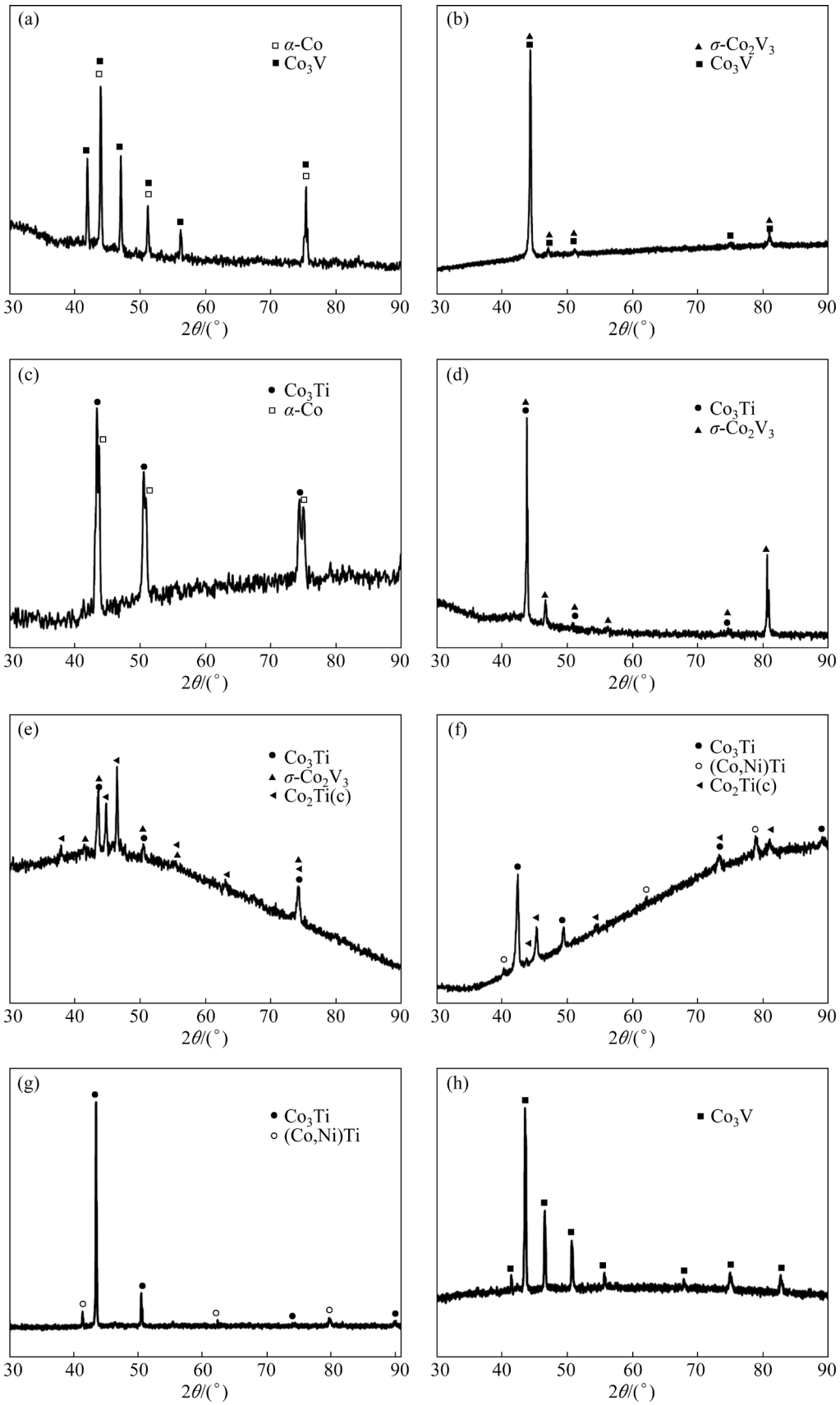

Fig. 4 XRD patterns of Co−10Ni−2Ti−19V (a), Co−20Ni−11Ti−20V (b), Co−10Ni−10Ti−10V (c), Co−15Ni−17Ti−18V (d), Co−10Ni−25Ti−5V (e), Co−15Ni−30Ti−1V (f), Co−20Ni−25Ti−5V (g), and Co−10Ni−9.5Ti−17.5V (h) alloys cold-rolled at reduction rate of 50% and annealed at 1000 °C

observed in the Co−10Ni−25Ti−5V alloy after annealing at 1000 °C for 120 d, as shown in Fig. 3(e). The white phase was identified as Co_3Ti, the light gray phase as Co_2Ti (c), and the black phase as σ-Co_2V_3. The corresponding XRD pattern is shown in Fig. 4(e). The Co−15Ni−30Ti−1V alloy exhibited a three-phase equilibrium microstructure after annealing at 1000 °C for 75 d, as depicted in Fig. 3(f). XRD analysis identified the three equilibrium phases as the Co_3Ti, Co_2Ti(c), and (Co, Ni)Ti phases, as shown in Fig. 4(f). After annealing at 1000 °C for 75 d, a two-phase equilibrium microstructure was observed in the Co−20Ni−25Ti−5V alloy, as shown in Fig. 3(g). The two-phase equilibrium microstructure was identified as (Co,Ni)Ti and Co_3Ti phases by XRD analysis, as shown in Fig. 4(g). The Co_3Ti phase is represented by a light gray color, while the (Co,Ni)Ti phase is represented by a dark gray color. Figure 3(h) shows the single-phase equilibrium microstructure of Co−10Ni−9.5Ti−17.5V alloy, which is identified as Co_3V by XRD analysis (Fig. 4(h)).

3.1.3 Isothermal section of Co−Ni−Ti−V quaternary system

Due to the mutual solubility of Co and Ni, as well as their similar physicochemical properties [27−29], the Co−Ni−Ti−V phase diagram can be represented as a two-dimensional Co−*x*Ni−Ti−V pseudo-ternary isothermal phase diagram [22,25]. The Co−*x*Ni−Ti−V two-dimensional phase diagrams in Fig. 5 show the phase constitutions of Co−10Ni−Ti−V, Co−15Ni−Ti−V and Co−20Ni−Ti−V alloys. Partial ternary alloy data (white circles in Fig. 5) were obtained from the study conducted by LI et al [30]. The α-Co and Co_3Ti two-phase regions expand with increasing Ni content, consistent with the findings reported for Co−Ni−Al−Ta [22] and Co−Ni−Al−W [25] quaternary alloys. Furthermore, Fig. 6(a) shows the DSC heating curves of Co−*x*Ni−10Ti−10V (*x*=10, 15, 20) alloys, which are essential for evaluating their phase transitions and thermal stability. As the Ni content increases, the γ' (Co_3Ti) solvus temperature increases significantly. Co−10Ni−10Ti−10V, Co−15Ni−10Ti−10V and Co−20Ni−10Ti−10V alloys exhibit remarkable thermo- dynamic stability with γ' (Co_3Ti) solvus temperatures of 1222.4, 1232.7 and 1242.7 °C, respectively. Compared to Co−12Ti (1005 °C) [17], Co−4Ti−12V (1023 °C) [31],

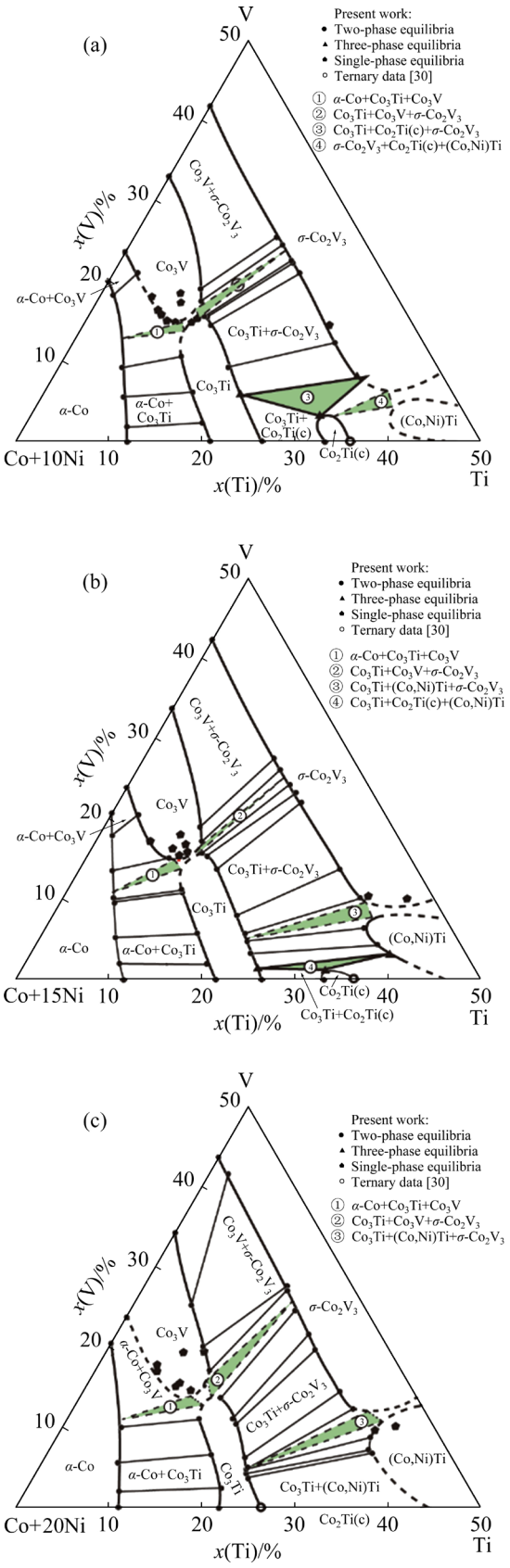

Fig. 5 Isothermal section diagrams of Co-rich regions of Co−10Ni−Ti−V (a), Co−15Ni−Ti−V (b), and Co−20Ni−Ti−V (c) systems at 1000 °C

Co−10Ti−11V (1103 °C) [32], and Co−9.2Al−9W (990 °C) [11] superalloys, the Co−10Ni−10Ti−10V alloy exhibits higher γ' solvus temperatures, with approximate increase of 22%, 19%, 11%, and 23%, respectively.

To further investigate the effect of Ni content, we plotted experimental phase diagrams (Fig. 6(b)) showing the curves of γ' solvus temperature, solid phase temperature, and liquid phase temperature as a function of Ni content in the Co−xNi−10Ti−10V longitudinal section. As the Ni content increases, the γ' solvus temperature and liquid phase temperature gradually increase, while the solid phase temperature changes slightly. At 20 at.% Ni, the γ' solvus temperature and the solidus temperature (~1248.6 °C) are very close, indicating that the Ni content is approaching the maximum limit for alloy design (a hot appropriate processing window should be provided to maintain operability). Furthermore, V is generally considered to increase the γ' solvus temperature [14,31,33]. Therefore, in Co−xNi−10Ti−10V (x=10, 15, 20) alloys, V content also approaches the maximum limit for alloy design.

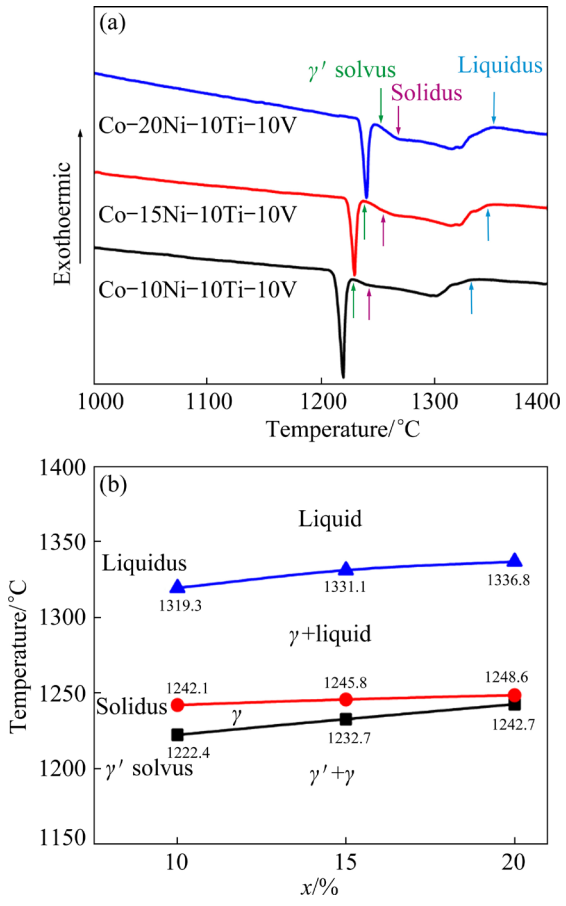

Fig. 6 DSC heating curves (a) and γ' solvus, solidus and liquidus temperatures (b) of Co−xNi−10Ti−10V (x=10, 15, 20) alloys

3.1.4 Partition coefficients of Co−Ni−Ti−V quaternary alloys

To quantitatively describe the partitioning tendencies of different elements in the γ (α-Co) and γ' (Co_3Ti) phases, the partition coefficients ($K_X^{\gamma'/\gamma}$) of each element can be expressed as follows:

$$K_X^{\gamma'/\gamma}=C_X^{\gamma'}/C_X^{\gamma} \quad (1)$$

where $C_X^{\gamma'}$ and C_X^{γ} represent the equilibrium compositions of element X in the γ' (Co_3Ti) and γ (α-Co) phases, respectively. Figures 7(a) and (b) illustrate the partition coefficients of each element X in the γ (α-Co) and γ' (Co_3Ti) phases of Co−xNi−15Ti−2V and Co−xNi−10Ti−10V (x=10, 15, 20) alloys at 1000 °C, respectively. If the partition coefficient is greater than 1, the element is a γ' phase forming element. Otherwise, the element becomes a γ phase forming element. In Co−xNi−15Ti−2V and Co−xNi−10Ti−10V (x=10, 15, 20) alloys, $K_V^{\gamma'/\gamma}$, $K_{Ni}^{\gamma'/\gamma}$, and $K_{Ti}^{\gamma'/\gamma}$ are always greater than 1, indicating that V, Ni and Ti elements tend to be distributed in the γ' phase, while the Co element tends to be distributed in the γ phase ($K_{Co}^{\gamma'/\gamma}$<1). Furthermore, it is worth noting that the partition coefficient for V ($K_V^{\gamma'/\gamma}$) remains relatively constant at different Ni contents.

3.2 Microstructure of Co−xNi−10Ti−10V quaternary alloys

To investigate the microstructure evolution of Co−Ni−Ti−V superalloys at intermediate to high temperatures, annealing experiments were performed on Co−xNi−10Ti−10V (x=10, 15, 20) alloys at 750 °C.

3.2.1 Lattice misfit

Lattice mismatch is a critical parameter in superalloys as it significantly impacts the stability of the γ' phase, coarsening behavior, and mechanical properties. The lattice parameter misfit (δ) is typically calculated using the following equation:

$$\delta=2(a_{\gamma'}-a_{\gamma})/(a_{\gamma'}+a_{\gamma}) \quad (2)$$

where $a_{\gamma'}$ and a_{γ} are the lattice parameters of the γ' phase and γ phase, respectively.

Figures 8(a−c) display the XRD diffraction peaks of the asymmetric (111) planes obtained from Co−10Ni−10Ti−10V, Co−15Ni−10Ti−10V, and Co−20Ni−10Ti−10V alloys after 48 h of aging. The

lattice mismatches in Co−10Ni−10Ti−10V, Co−15Ni−10Ti−10V and Co−20Ni−10Ti−10V alloys are measured as 0.34%, 0.28% and 0.20%, respectively. To further explore the correlation between the lattice parameters of the γ' and γ phases and the magnitude of the lattice mismatch with respect to the Ni content, plots are shown in Figs. 8(d, e). As the Ni content increases, there is a significant decrease in the lattice parameter of the γ' phase while the decrease in the lattice parameter of the γ phase is subtle. This finding is consistent with the study conducted by ZHOU et al [33]. This phenomenon is primarily due to the tendency of Ni atoms to concentrate within the γ' phase, along with their markedly smaller atomic radius compared to Ti and V, which leads to a considerable reduction in the γ' phase lattice parameter. Meanwhile, the Ni atomic radius is only slightly smaller than that of Co, resulting in a minor decrease in the lattice constant of the γ phase (with atomic radii of 1.252, 1.244, 1.467, and 1.338 Å for Co, Ni, Ti, and V, respectively) [34,35].

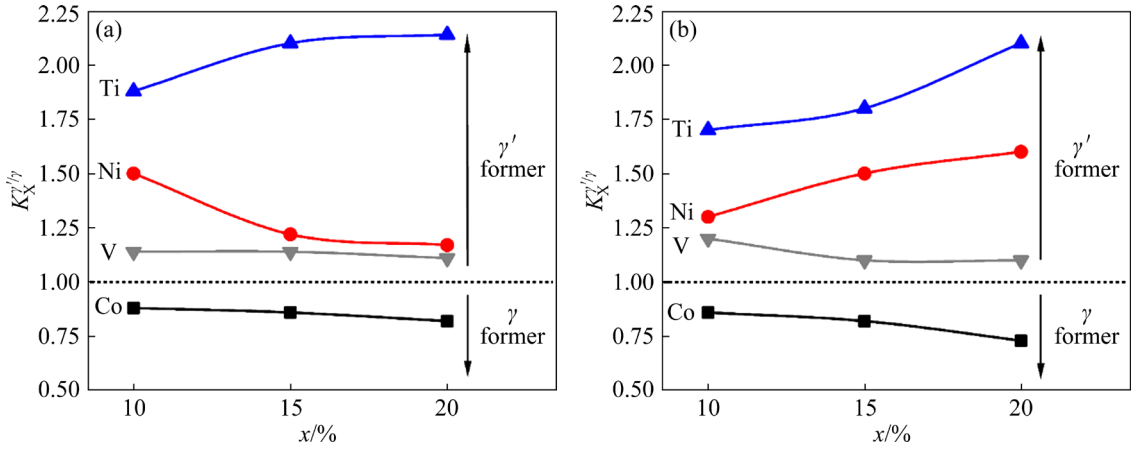

Fig. 7 Variation of partition coefficient $K_X^{\gamma'/\gamma}$ for each element in Co−xNi−10Ti−10V (a) and Co−xNi−15Ti−2V (b) (x=10, 15, 20) alloys at 1000 °C

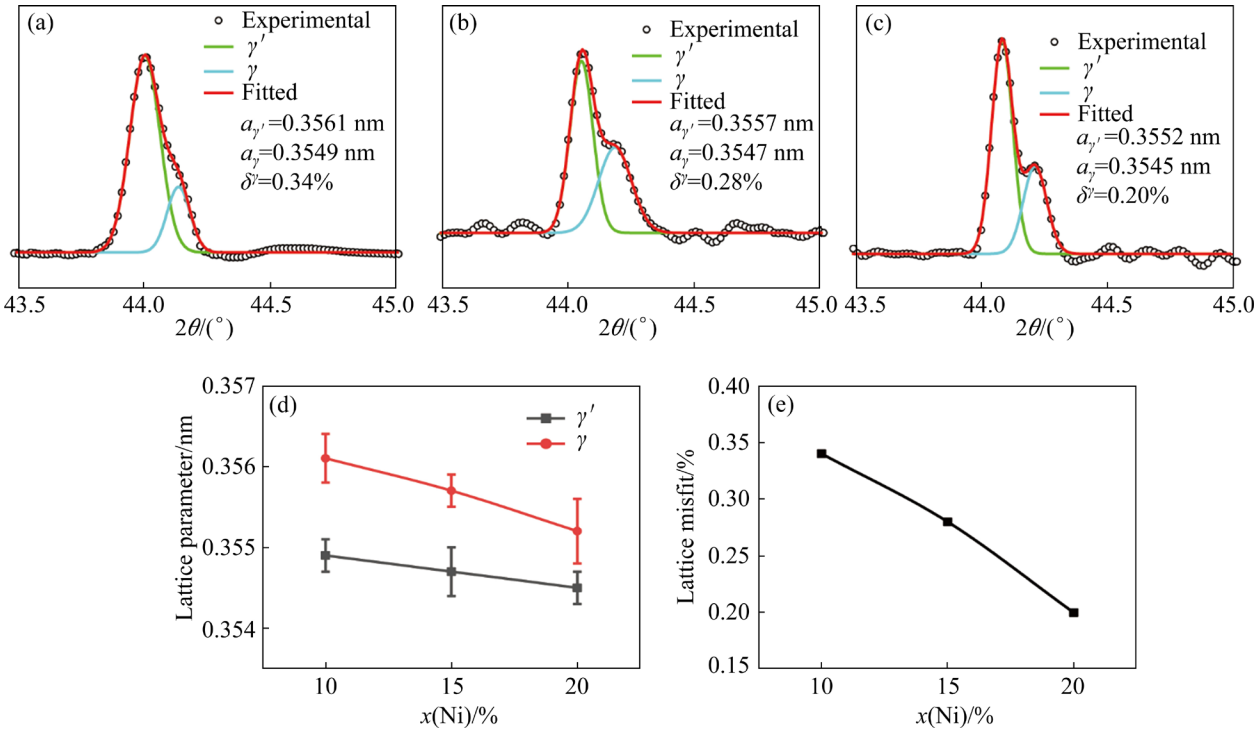

Fig. 8 Typical asymmetric XRD peaks of (111) planes for Co−10Ni−10Ti−10V (a), Co−15Ni−10Ti−10V (b) and Co−20Ni−10Ti−10V (c) alloys, variation of lattice parameters of γ' and γ phases with Ni content (d), and comparison of γ'/γ lattice mismatch with different Ni contents (e)

3.2.2 Coarsening behavior of γ' phase

Figure 9 illustrates the morphological changes of γ' precipitates in the Co−xNi−10Ti−10V (x=10, 15, 20) alloys after aging at 750 °C for 24−192 h. The γ' precipitates in all samples show a cubic shape, indicating excellent microstructural stability of the γ' precipitates at 750 °C.

There are various models for coarsening regular γ' precipitates, with two prominent ones being the LSW model and the trans-interface diffusion-controlled coarsening (TIDC) model. The LSW model describes the coarsening of γ' precipitates in a γ matrix via diffusion-controlled growth [36−38], while the TIDC model is focused on systems that involve order/disorder interfaces, where solute diffusion across an ordered interface can be rate-limiting instead of solute diffusion through the disordered matrix [39]. The kinetics of coarsening is described as

$$[r(t)]^n-[r(t_0)]^n=K(t-t_0) \quad (3)$$

where $r(t)$ represents the average γ' precipitate radius at specific time t, $r(t_0)$ represents the average γ' precipitate radius at initial time t_0, K is the coarsening rate coefficient of γ' precipitate, while temporal exponent n is a key parameter. For LSW, the value of n is typically equal to 3, while for TIDC, it is 2.

Figure 10(a) depicts the use of multivariable linear regression to analyze the relationship between

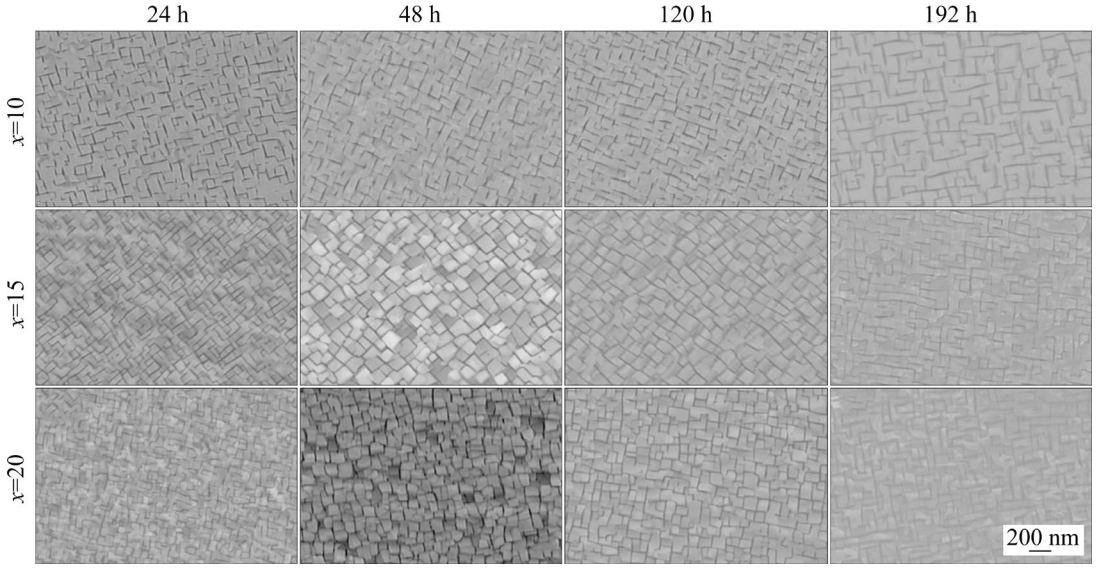

Fig. 9 Secondary electron SEM images of Co−xNi−10Ti−10V (x=10, 15, 20) alloys showing temporal evolution of γ/γ' microstructure during aging at 750 °C for 24−192 h

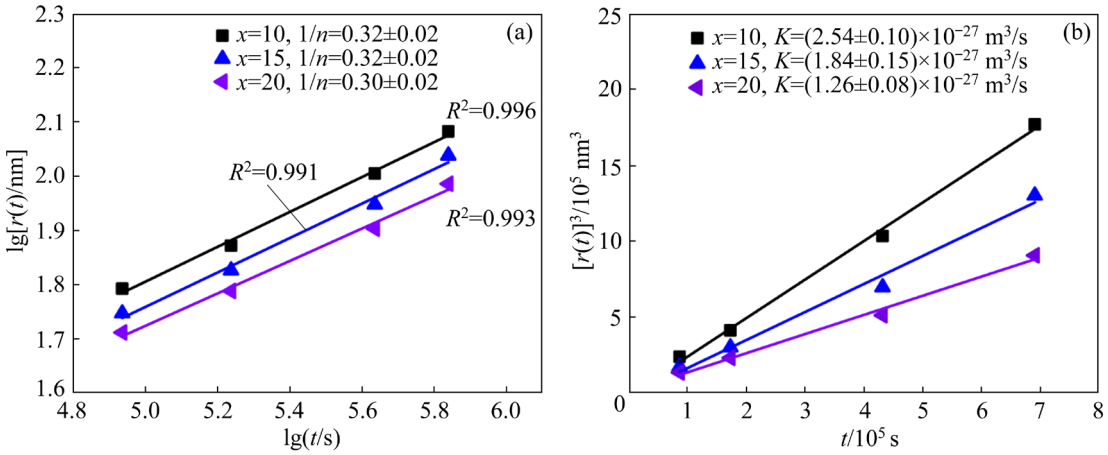

Fig. 10 Plots between lg [$r(t)$] vs lg t giving temporal exponents of average precipitate radius evolution (a), and plots between $[r(t)]^3$ vs t with linear regression analysis to datasets giving slope values corresponding to coarsening rate constants K (b) of Co−xNi−10Ti−10V alloys

lg[$r(t)$] and lg t, and provides the inverse of temporal exponent (1/n). The slope values (1/n) of the curve were determined to be 0.32±0.02, 0.32±0.02, and 0.30±0.02 for the Co−10Ni−10Ti−10V, Co−15Ni−10Ti−10V, and Co−20Ni−10Ti−10V alloys, respectively. These results suggest that the LSW model is a suitable description for the coarsening behavior of γ' precipitates in this system.

Figure 10(b) displays plots of $[r(t)]^3$ versus t, with the coarsening rate (K) at 750 °C obtained by performing multiple linear regression analysis. The coarsening rates of the Co−10Ni−10Ti−10V, Co−15Ni−10Ti−10V, and Co−20Ni−10Ti−10V alloys are (2.54±0.10)×10^{-27} m^3/s, (1.84±0.15)×10^{-27} m^3/s, and (1.26±0.08)×10^{-27} m^3/s, respectively, indicating that the addition of Ni effectively reduces the coarsening rate. The coarsening rate of Co−Ti-based superalloys with high Ti content is generally 1−2 orders of magnitude higher than that of Ni-based and Co−Al−X-based superalloys [40−43]. In contrast, the coarsening rate of the Co−20Ni−10Ti−10V alloy is comparable to that of the Inconel 939 superalloy (2.67×$10^{-27}$$m^3$/s at 750 °C) [44].

There are two main factors that affect the coarsening rate, namely diffusion coefficient and γ/γ' lattice mismatch [45−47]. Currently, there are few reports on the diffusion coefficients of quaternary alloys, and even less is known about the diffusion coefficients of Co−Ni−Ti−V quaternary alloys. The increased Ni content in Co−xNi−10Ti−10V (x=10, 15, 20) alloys may hinder the interdiffusion coefficients of other atoms, leading to a reduced coarsening rate of the γ' phase. On the other hand, reducing the lattice mismatch between γ and γ' can decrease the coherent strain energy at their interface, which directly affects both the high-temperature mechanical properties and coarsening behavior.

3.3 Density and mechanical performance of Co−xNi−10Ti−10V quaternary alloys

The densities of Co−10Ni−10Ti−10V, Co−15Ni−10Ti−10V, Co−20Ni−10Ti−10V, Co−12Ti, Co−4Ti−12V, Co−11Ti−15Cr, and Co−9.2Al−9W superalloys are compared in Fig. 11(a).

The Co−10Ni−10Ti−10V, Co−15Ni−10Ti−10V and Co−20Ni−10Ti−10V alloys exhibit similar densities at approximately 8.07 g/cm^3. Compared to Co−12Ti (8.30 g/cm^3) [19], Co−4Ti−12V (8.23 g/cm^3) [31], and Co−9.2Al−9W (9.54 g/cm^3) [48], the Co−xNi−10Ti−10V alloys show a decrease in density of approximately 3%, 2%, and 15%, respectively.

Figure 11(b) illustrates the correlation between the hardness and aging time at 750 °C for Co−10Ni−10Ti−10V, Co−15Ni−10Ti−10V, and Co−20Ni−10Ti−10V alloys. Compared to homogeneous alloys, the hardness of annealed alloys significantly increases, indicating that the precipitated γ' phase contributes to the improved hardness. Furthermore, the peak hardness values of Co−10Ni−10Ti−10V, Co−15Ni−10Ti−10V, and Co−20Ni−10Ti−10V alloys are HV (440±12), HV (459±8), and HV (467±4), respectively. Compared to Co−4Ti−12V (HV 408, 8.23 g/cm^3) [31] and Co−12Ti−1Re (HV 428, 8.41 g/cm^3) [20] alloys, Co−10Ni−10Ti−10V, Co−15Ni−10Ti−10V, and Co−20Ni−10Ti−10V alloys exhibit higher hardness, highlighting the potential for future development of Co−Ni−Ti−V alloys [49−51].

In addition, in this study, the mechanical properties of Co−xNi−10Ti−10V alloys were also examined using high-temperature compression tests to assess the temperature dependence of the yield strength. Figure 11(c) shows the temperature dependence of the yield strength of Co−10Ni−10Ti−10V, Co−15Ni−10Ti−10V, Co−20Ni−10Ti−10V, Co−2Ni−5Ti−15V [14] and Co−11Ti−15Cr [19] alloys. Abnormal yielding was observed for Co−10Ni−10Ti−10V, Co−15Ni−10Ti−10V, and Co−20Ni−10Ti−10V alloys near 700 °C. At room temperature, the yield strength of the Co−10Ni−10Ti−10V, Co−15Ni−10Ti−10V, and Co−20Ni−10Ti−10V alloys were measured as (658±8), (747±30), and (820±20) MPa, respectively. When tested at 700 °C, the yield strengths were determined to be (680±20), (702±25), and (720±20) MPa for the respective alloys. At 1000 °C, the alloys exhibited yield strengths of (478±9), (520±40), and (508±12) MPa, respectively.

Compared to the Co−2Ni−5Ti−15V and Co−11Ti−15Cr lightweight superalloys, the Co−10Ni−10Ti−10V, Co−15Ni−10Ti−10V and Co−20Ni−10Ti−10V alloys exhibit excellent mechanical properties in the medium to high temperature range. Co−10Ni−10Ti−10V, Co−15Ni−10Ti−10V and Co−20Ni−10Ti−10V alloys show significant variations in their yield strengths from room temperature to 700 °C. However, at higher temperatures, their yield strengths become quite

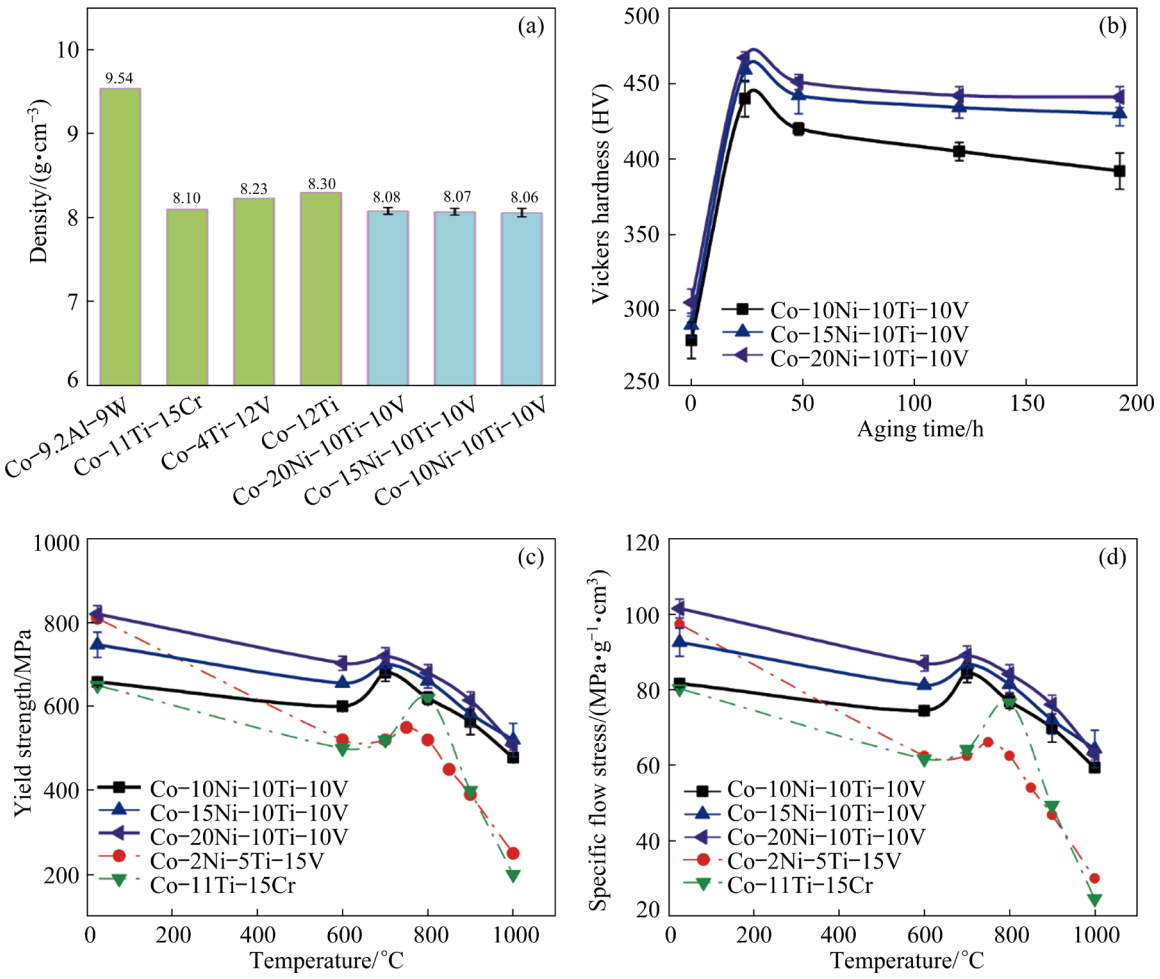

Fig. 11 Density comparison of Co−*x*Ni−10Ti−10V (*x*=10, 15, 20), Co−12Ti, Co−4Ti−12V, Co−11Ti−15Cr, and Co−9.2Al−9W alloys (a), aging time dependence of hardness in Co−*x*Ni−10Ti−10V (*x*=10, 15, 20) alloys at 750 °C (b), and nominal yield strength (c) and specific yield strength (d) versus temperatures curves of Co−*x*Ni−10Ti−10V (*x*=10, 15, 20), Co−2Ni−5Ti−15V and Co−11Ti−15Cr alloys, respectively

similar. This indicates that the presence of the Ni element plays a critical role in influencing the yield strength in the range of room temperature to 700 °C, but it doesn't have a noticeable impact on improving the yield strength at higher temperatures. Co−*x*Ni−10Ti−10V (*x*=10, 15, 20) alloys exhibit exceptional high-temperature yield strength, which can be attributed to several factors, including their high γ' phase fraction, elevated γ' solvus temperature, and low γ/γ' misfit. Furthermore, it is worth noting that the Co−*x*Ni−10Ti−10V (*x*=10, 15, 20) series alloys exhibit minor variations in yield strength with temperature. This observation suggests that this series of alloys have excellent microstructural stability at elevated temperatures, promising them for a wide range of applications. Figure 11(d) shows the variation of specific yield strength with temperature for Co−*x*Ni−10Ti−10V (*x*=10, 15, 20), Co−2Ni−5Ti−15V [14] and Co−11Ti−15Cr [19] alloys.

In order to better understand the underlying factors contributing to the remarkable mechanical properties of Co−20Ni−10Ti−10V alloys at high temperatures, a detailed microstructural analysis was carried out. The analysis focused on Co−20Ni−10Ti−10V alloys with 1% strain at 1000 °C, as depicted in Fig. 12. Under a strain rate of 1×10^{-4} s^{-1}, the defect structure observed in the Co−20Ni−10Ti−10V alloy is predominantly characterized by a high density of stacking faults (indicated by red arrows). Additionally, a few APB-coupled dislocation pairs can be observed (indicated by white arrows). It is indicated that the deformation mechanism in the Co−20Ni−10Ti−10V alloy involves a combination of stacking fault shear and APB-coupled dislocation pair shear, resembling

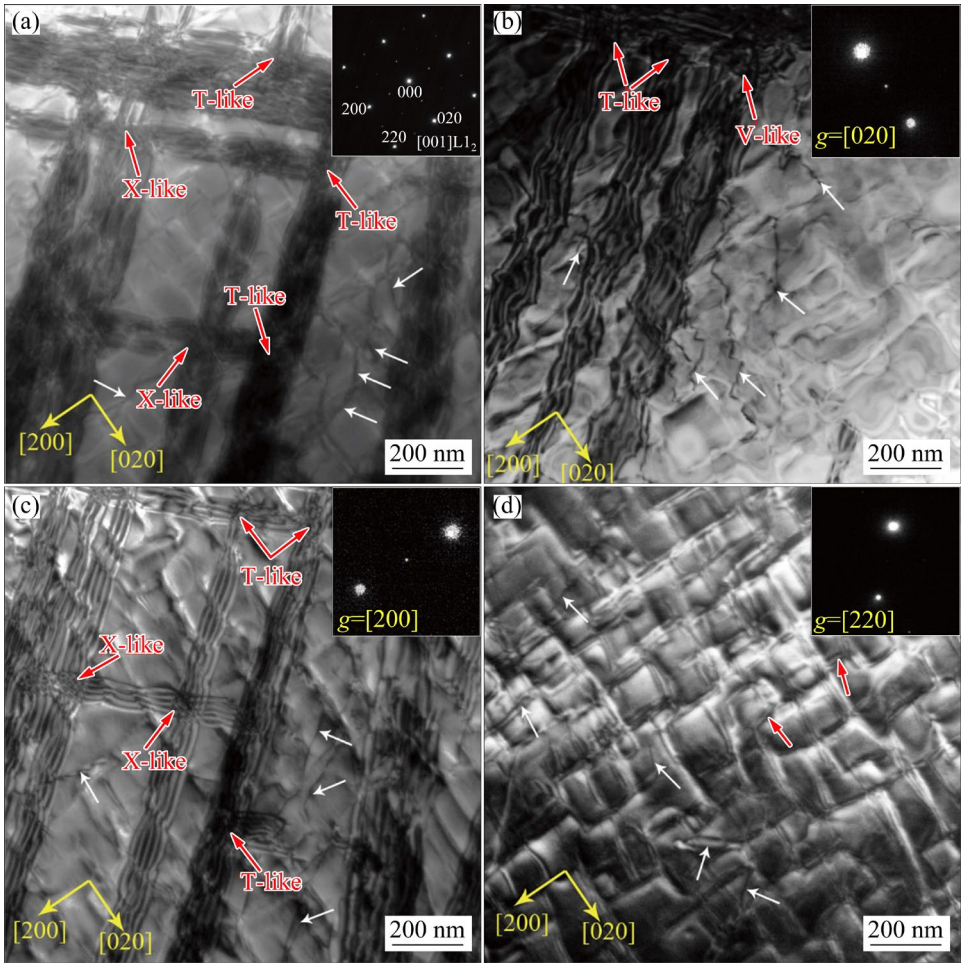

Fig. 12 TEM images of Co−20Ni−10Ti−10V alloy after interrupted compression experiments at plastic strain of about 1% and temperature of 1000 °C: (a) Bright-field image in [001] zone axis; (b, c, d) Central dark-field images using g=[020], g=[200], and g=[220], respectively

the mechanism of Co−Ti−Cr alloys [52,53]. Furthermore, it is suggested that the deformation mechanism may undergo a transformation from APB-coupled dislocation pair shear to stacking fault shear during the deformation process [54]. The presence of a high density of stacking fault shear in the Co−20Ni−10Ti−10V alloy at 1000 °C is believed to contribute to its exceptional mechanical properties, consistent with findings in CoNi-based superalloys [54−56].

4 Conclusions

(1) The γ and γ' two-phase regions expand significantly with increasing Ni content in the Co−xNi−Ti−V (x=10, 15, 20) phase diagrams.

(2) The γ' solvus temperature and thermal stability of Co−xNi−10Ti−10V (x=10, 15, 20) alloys improve with increasing Ni content. Notably, Co−20Ni−10Ti−10V alloy demonstrates a high γ' solvus temperature of approximately 1242.7 °C.

(3) Co−xNi−10Ti−10V (x=10, 15, 20) alloys were prepared, and as the Ni content increased, the mass density varied slightly. In addition, the coarsening rate of γ' precipitates and the lattice mismatch between γ and γ' phases decreased.

(4) The Co−xNi−10Ti−10V (x=10, 15, 20) alloys exhibit excellent mechanical performance at high temperatures. At 1000 °C, the yield strength of Co−10Ni−10Ti−10V is (478±9) MPa, Co−15Ni−10Ti−10V is (520±40) MPa, and Co−20Ni−10Ti−10V is (508±12) MPa. Notably, the presence of high-density stacking fault shear in the Co−20Ni−10Ti−10V alloy is believed to be the reason for its outstanding mechanical performance at 1000 °C.

CRediT authorship contribution statement

Jian-ping LE: Methodology, Validation, Formal analysis, Investigation, Data curation, Writing − Original draft; **Jin-bin ZHANG:** Resources, Supervision; **Yu-peng ZHANG:** Methodology, Formal analysis; **Yi-hui GUO:** Methodology, Formal analysis; **Yong LU:** Writing − Review & editing, Supervision; **Cui-ping WANG:** Conceptualization, Resources, Supervision, Writing − Review & editing, Supervision, Project administration, Funding acquisition; **Xing-jun LIU:** Conceptualization, Resources, Project administration, Funding acquisition.

Declaration of competing interest

The authors declare that they have no known competing financial interests or personal relationships that could have appeared to influence the work reported in this paper.

Acknowledgments

This study was supported by the National Natural Science Foundation of China (Nos. 51831007, 52371007), the Shenzhen Science and Technology Program, China (No. SGDX20210823104002016), and the Guangdong Basic and Applied Basic Research Foundation, China (No. 2021B1515120071).

Data availability

The original contributions presented in the study are included in the article/Supplementary Materials, further inquiries can be directed to the corresponding authors.

Supplementary Materials

Supplementary Materials in this paper can be found at: http://tnmsc.csu.edu.cn/download/16-p3795-2024-0383-Supplementary_Materials.pdf.

References

[1] SMITH T M, RAO Y, WANG Y, GHAZISAEIDI M, MILLS M J. Diffusion processes during creep at intermediate temperatures in a Ni-based superalloy [J]. Acta Materialia, 2017, 141: 261−272.

[2] POLLOCK T M. Alloy design for aircraft engines [J]. Nature Materials, 2016, 15: 809−815.

[3] LIU Xing-jun, CHEN Yue-chao, LU Yong, HAN Jia-jia, XU Wei-wei, GUO Yi-hui, YU Jin-xin, WEI Zhen-bang, WANG Cui-ping. Present research situation and prospect of multi-scale design in novel Co-based superalloys: A review [J]. Acta Metallurgica Sinica, 2020, 56: 1−20.

[4] WINOWLIN JAPPES J T, AJITHRAM A, ADAMKHAN M, REENA D. Welding on Ni based super alloys—A review [J]. Materials Today: Proceedings, 2022, 60: 1656−1659.

[5] ZHU Qiang, CHEN Lin-jun, CHEN Gang, WANG Chuan-jie, QIN He-yong, ZHANG Peng. A two-stage constitutive model and microstructure evolution simulation of a nickel-based superalloy during high temperature deformation [J]. Journal of Materials Engineering and Performance, 2023, 32: 3378−3389.

[6] JAMES A W, RAJAGOPALAN S. Gas turbines: Operating conditions, components and material requirements [M]. Sawston, Cambridge: Woodhead Publishing, 2014.

[7] PEREPEZKO J H. The hotter the engine, the better [J]. Science, 2009, 326: 1068−1069.

[8] YAMAGUCHI M, INUI H, ITO K. High-temperature structural intermetallics [J]. Acta Materialia, 2000, 48: 307−322.

[9] LEMBERG J A, RITCHIE R O. Mo−Si−B alloys for ultrahigh-temperature structural applications [J]. Adv Mater, 2012, 24: 3445−3480.

[10] VIATOUR P, DRAPIER J, COUTSOURADIS D. Stability of the γ'-Co_3Ti compound in simple and complex cobalt alloys [J]. Cobalt, 1973, 3: 67−74.

[11] SATO J, OMORI T, OIKAWA K, OHNUMA I, KAINUMA R, ISHIDA K. Cobalt-base high-temperature alloys [J]. Science, 2006, 312: 90−91.

[12] BLAISE J, VIATOUR P, DRAPIER J. On the stability and precipitation of the Co_3Ti phase in Co−Ti alloys [J]. Cobalt, 1970, 49: 192−195.

[13] JIANG Min, SAREN G, YANG Su-yu, LI Hong-xiao, HAO Shi-ming. Phase equilibria in Co-rich region of Co−Ti−Ta system [J]. Transactions of Nonferrous Metals Society of China, 2011, 21: 2391−2395.

[14] RUAN J J, LIU X J, YANG S Y, XU W W, OMORI T, YANG T, DENG B, JIANG H X, WANG C P, KAINUMA R, ISHIDA K. Novel Co−Ti−V-base superalloys reinforced by L12-ordered γ' phase [J]. Intermetallics, 2018, 92: 126−132.

[15] RUAN Jing-jing, WANG Cui-ping, ZHAO Can-can, YANG Shui-yuan, YANG Tao, LIU Xing-jun. Experimental investigation of phase equilibria and microstructure in the Co−Ti−V ternary system [J]. Intermetallics, 2014, 49: 121−131.

[16] IM H J, LEE S B, CHOI W S, MAKINENI S K, RAABE D, KO W S, CHOI P P. Effects of Mo on the mechanical behavior of γ/γ'-strengthened Co−Ti-based alloys [J]. Acta Materialia, 2020, 197: 69−80.

[17] IM H J, MAKINENI S K, GAULT B, STEIN F, RAABE D, CHOI P P. Elemental partitioning and site-occupancy in γ/γ' forming Co−Ti−Mo and Co−Ti−Cr alloys [J]. Scripta Materialia, 2018, 154: 159−162.

[18] YOO B, IM H J, SEOL J B, CHOI P P. On the microstructural evolution and partitioning behavior of L12-structured γ'-based Co−Ti−W alloys upon Cr and Al alloying [J]. Intermetallics, 2019, 104: 97−102.

[19] ZENK C H, POVSTUGAR I, LI R, RINALDI F, NEUMEIER S, RAABE D, GÖKEN M. A novel type of Co−Ti−Cr-base γ/γ' superalloys with low mass density [J]. Acta Materialia, 2017, 135: 244−251.

[20] LI Ling-ling, WANG Cui-ping, CHEN Yue-chao, YANG Shui-yuan, YANG Mu-jin, ZHANG Jin-bin, LU Yong, HAN Jia-jia, LIU Xing-jun. Effect of Re on microstructure and

mechanical properties of γ/γ′ Co-Ti-based superalloys [J]. Intermetallics, 2019, 115: 106612.

[21] LI Ling-ling, WANG Cui-ping, YANG Shui-yuan, HAN Jia-jia, LU Yong, ZHANG Jin-bin, LIU Xing-jun. Phase equilibria in Co−Ti−Re ternary system [J]. Rare Metals, 2023, 42: 2736−2746.

[22] CHEN Yue-chao, WANG Cui-ping, RUAN Jing-jing, YANG Shui-yuan, OMORI T, KAINUMA R, ISHIDA K, HAN Jia-jia, LU Yong, LIU Xing-jun. Development of low-density γ/γ′ Co−Al−Ta-based superalloys with high solvus temperature [J]. Acta Materialia, 2020, 188: 652−664.

[23] CAO B X, XU W W, YU C Y, WU S W, KONG H J, DING Z Y, ZHANG T L, LUAN J H, XIAO B, JIAO Z B, LIU Y, YANG T, LIU C T. L12-strengthened multicomponent Co−Al−Nb-based alloys with high strength and matrix-confined stacking-fault-mediated plasticity [J]. Acta Materialia, 2022, 229: 117763.

[24] CHEN Yue-chao, WANG Cui-ping, RUAN Jing-jing, OMORI T, KAINUMA R, ISHIDA K, LIU Xing-jun. High-strength Co−Al−V-base superalloys strengthened by γ′-Co_3(Al,V) with high solvus temperature [J]. Acta Materialia, 2019, 170: 62−74.

[25] SHINAGAWA K, OMORI T, SATO J, OIKAWA K, OHNUMA I, KAINUMA R, ISHIDA K. Phase equilibria and microstructure on γ′ phase in Co−Ni−Al−W system [J]. Materials Transactions, 2008, 49: 1474−1479.

[26] WANG Cui-ping, LE Jian-ping, CHEN Ke-ying, YANG Chen, YU Jin-xin, GUO Yi-hui, ZHUO Hao-jun, ZHANG Jin-bin, HAN Jia-jia, LIU Xing-jun. A novel Co−Ni−Ti−V-based superalloy exhibiting low density and high strength [J]. Materials Science and Engineering A, 2023, 885: 145633.

[27] LIU Mao-cheng, KONG Ling-bin, KANG Long, LI Xiao-hong, WALSH F C, XING Man, LU Chao, MA Xue-jing, LUO Yong-chun. Synthesis and characterization of $M_3V_2O_8$ (M = Ni or Co) based nanostructures: a new family of high performance pseudocapacitive materials [J]. Journal of Materials Chemistry A, 2014, 2: 4919−4926.

[28] NISHIZAWA T, ISHIDA K. The Co−Ni (cobalt−nickel) system [J]. Bulletin of Alloy Phase Diagrams, 1983, 4: 390−395.

[29] ZHANG Jing-chao, YUAN Bai-qing, CUI Shu-fang, ZHANG Na-na, WEI Jing-jing, WANG Xiao, ZHANG Dao-jun, ZHANG Ren-chun, HUO Qi-sheng. Facile synthesis of 3D porous $Co_3V_2O_8$ nanoroses and 2D $NiCo_2V_{2O8}$ nanoplates for high performance supercapacitors and their electrocatalytic oxygen evolution reaction properties [J]. Dalton Transactions, 2017, 46: 3295−3302.

[30] LI Han, ZHOU Peng, DU Yong, JIN Zhan-peng. Isothermal sections of the Co−Ni−Ti system at 950 and 1000 °C [J]. International Journal of Materials Research, 2018, 109: 105−112.

[31] LIU Xing-jun, PAN Yun-wei, CHEN Yue-chao, HAN Jia-jia, YANG Shui-yuan, RUAN Jing-jing, WANG Cui-ping, YANG Yuan-shen, LI Ying-ju. Effects of Nb and W additions on the microstructures and mechanical properties of novel γ/γ′ Co−V−Ti−based superalloys [J]. Metals, 2018, 8: 563−574.

[32] ZHOU Peng-jie, GAO Xin-kang, SONG De-hang, LIU Qi-long, LIU Yin-bing, CHENG Jun. Role of Ru on the microstructure and property of novel Co−Ti−V Superalloy [J]. Journal of Materials Research, 2020, 35: 2737−2745.

[33] ZHOU Peng-jie, GAO Xin-kang, SONG De-hang, LIU Yin-bing, CHENG Jun, BUZIO R. Effect of Ni on microstructure and mechanical property of a Co−Ti−V-based superalloy [J]. Scanning, 2021, 2021: 6678085.

[34] PAULING L. Atomic radii and interatomic distances in metals [J]. Journal of the American Chemical Society, 1947, 69: 542−553.

[35] SLATER J C. Atomic radii in crystals [J]. The Journal of Chemical Physics, 1964, 41: 3199−3204.

[36] CALDERON H A, VOORHEES P W, MURRAY J L, KOSTORZ G. Ostwald ripening in concentrated alloys [J]. Acta Metallurgica et Materialia, 1994, 42: 991−1000.

[37] KUEHMANN C J, VOORHEES P W. Ostwald ripening in ternary alloys [J]. Metallurgical and Materials Transactions A, 1996, 27: 937−943.

[38] PHILIPPE T, VOORHEES P W. Ostwald ripening in multicomponent alloys [J]. Acta Materialia, 2013, 61: 4237−4244.

[39] ARDELL A J, OZOLINS V. Trans-interface diffusion-controlled coarsening [J]. Nature Materials, 2005, 4: 309−316.

[40] LASS E A, SAUZA D J, DUNAND D C, SEIDMAN D N. Multicomponent γ′-strengthened Co-based superalloys with increased solvus temperatures and reduced mass densities [J]. Acta Materialia, 2018, 147: 284−295.

[41] VORONTSOV V A, BARNARD J S, RAHMAN K M, YAN H Y, MIDGLEY P A, DYE D. Coarsening behaviour and interfacial structure of γ′ precipitates in Co−Al−W based superalloys [J]. Acta Materialia, 2016, 120: 14−23.

[42] SAUZA D J, BOCCHINI P J, DUNAND D C, SEIDMAN D N. Influence of ruthenium on microstructural evolution in a model CoAlW superalloy [J]. Acta Materialia, 2016, 117: 135−145.

[43] MUKHOPADHYAY S, PANDEY P, BALER N, BISWAS K, MAKINENI S K, CHATTOPADHYAY K. The role of Ti addition on the evolution and stability of γ/γ′ microstructure in a Co−30Ni−10Al−5Mo−2Ta alloy [J]. Acta Materialia, 2021, 208: 116736.

[44] FOOTNER P K, RICHARDS B P. Long-term growth of superalloy γ′ particles [J]. Journal of Materials Science, 1982, 17: 2141−2153.

[45] HE Chuang, LIU Lin, HUANG Tai-wen, YANG Wen-chao, WANG Xiao-jun, ZHANG Jun, GUO Min, FU Heng-zhi. The effects of misfit and diffusivity on γ′ rafting in Re and Ru containing Nickel based single crystal superalloys-details in thermodynamics and dynamics [J]. Vacuum, 2021, 183: 109839.

[46] HE Feng, ZHANG Kai-wei, YELI G, TONG Yang, WEI Dai-xiu, LI Jun-jie, WANG Zhi-jun, WANG Jin-cheng, KAI Ji-jung. Anomalous effect of lattice misfit on the coarsening behavior of multicomponent L12 phase [J]. Scripta Materialia, 2020, 183: 111−116.

[47] ZHUANG Xiao-li, ANTONOV S, LI Long-fei, FENG Qiang. Effect of alloying elements on the coarsening rate of γ′ precipitates in multi-component CoNi-based superalloys with high Cr content [J]. Scripta Materialia, 2021, 202: 114004.

[48] SHI L, YU J J, CUI C Y, SUN X F. Microstructural stability and tensile properties of a Ti-containing single-crystal Co−Ni−Al−W-base alloy [J]. Materials Science and Engineering: A, 2015, 646: 45−51.
[49] ZHANG P, LI S X, ZHANG Z F. General relationship between strength and hardness [J]. Materials Science and Engineering: A, 2011, 529: 62−73.
[50] RAO K L, GUPTA A K. Mechanical and microstructural characterization of Nimonic 263 superalloy after constrained groove pressing at elevated temperatures [J]. Materials Characterization, 2023, 203: 113157.
[51] WHITMORE L, AHMADI M R, GUETAZ L, LEITNER H, POVODEN-KARADENIZ E, STOCKINGER M, KOZESCHNIK E. The microstructure of heat-treated nickel-based superalloy 718Plus [J]. Materials Science and Engineering: A, 2014, 610: 39−45.
[52] BEZOLD A, VOLZ N, LENZ M, ZENK C H, SPIECKER E, MILLS M, GÖKEN M, NEUMEIER S. Yielding behavior of a single-crystalline γ′-strengthened Co−Ti−Cr superalloy [J]. Scripta Materialia, 2021, 200: 113928.
[53] SHI L, YU J J, CUI C Y, SUN X F. Temperature dependence of deformation behavior in a Co−Al−W-base single crystal superalloy [J]. Materials Science and Engineering: A, 2015, 620: 36−43.
[54] BEZOLD A, NEUMEIER S. Tailoring deformation mechanisms in polycrystalline CoNi-base superalloys for enhanced high temperature strength [J]. Scripta Materialia, 2023, 226: 115250.
[55] QU Sha-sha, LI Ying-ju, HE Ming-lin, WANG Cui-ping, LIU Xing-jun, CHEN Yue-chao, YANG Yuan-shen. Microstructural evolution and compression property of a novel γ′-strengthened directionally solidified CoNi-base superalloy [J]. Materials Science and Engineering A, 2019, 761: 138034.
[56] YANG Wen-chao, QU Peng-fei, LIU Chen, CAO Kai-li, QIN Jia-run, SU Hai-jun, ZHANG Jun, REN Cui-dong, LIU Lin. Temperature dependence of compressive behavior and deformation microstructure of a Ni-based single crystal superalloy with low stacking fault energy [J]. Transactions of Nonferrous Metals Society of China, 2023, 33(1): 157−167.

基于相图开发具有优异高温强度的 Co−Ni−Ti−V 高温合金

乐建平[1,2]，张锦彬[1,2]，张玉朋[1,2]，郭毅慧[1,2]，卢 勇[1,2]，王翠萍[1,2]，刘兴军[3]

1. 厦门大学 材料学院 福建省材料基因工程重点实验室，厦门 361005；
2. 厦门大学 厦门市高性能金属材料重点实验室，厦门 361005；
3. 哈尔滨工业大学 材料基因与大数据研究院，深圳 518055

摘 要：采用电子探针 X 射线显微分析 (EPMA)和 X 射线衍射(XRD)等表征技术研究 Co−Ni−Ti−V 四元系富 Co−Ni 区的相平衡，建立了在 1000 ℃下 3 个四元体系 Co−10Ni−Ti−V、Co−15Ni−Ti−V 和 Co−20Ni−Ti−V 的等温截面。研究结果表明，随着镍含量的增加，γ (α-Co)和 γ′(Co_3Ti)两相区的成分范围明显扩大。基于 Co−Ni−Ti−V 相图，设计了具有高 γ′溶解温度的合金，并对其进行了全面的性能评估，包括 γ′相粗化行为和力学性能。相较于 Co−Ti 二元合金，所设计的 Co−20Ni−10Ti−10V 合金展现了较低的 γ′相粗化速率以及较小的 γ/γ′两相晶格错配度。值得注意的是，该合金具有优异的高温力学性能，在 1000 ℃时的屈服强度为 508 MPa。这种优异性能主要归因于合金内部存在高密度的堆垛层错剪切。

关键词：Co−Ni−Ti−V；相平衡；分配系数；粗化速率；力学性能

(Edited by Xiang-qun LI)